The magnetic structure of convection-driven numerical dynamos

Julien Aubert, Jonathan Aurnou, Johannes Wicht

HAL Id: hal-00365069
https://hal.science/hal-00365069

Submitted on 7 Aug 2020

The magnetic structure of convection-driven numerical dynamos

Julien Aubert,[1] Jonathan Aurnou[2] and Johannes Wicht[3]

[1]*Dynamique des Fluides Géologiques, Institut de Physique du Globe de Paris,* 4 *place Jussieu,* 75252 *Paris cedex 5, France. E-mail: aubert@ipgp.jussieu.fr*
[2]*Department of Earth and Space Sciences, University of California, Los Angeles, USA*
[3]*Max-Planck Institute for Solar System Research, Katlenburg-Lindau, Germany*

SUMMARY

The generation of a magnetic field in numerical simulations of the geodynamo is an intrinsically 3-D and time-dependent phenomenon. The concept of magnetic field lines and the frozen-flux approximation can provide insight into such systems, but a suitable visualization method is required. This paper presents results obtained using the Dynamical Magnetic Field line Imaging (DMFI) technique, which is a representation of magnetic field lines accounting for their local magnetic energy, together with an algorithm for the time evolution of their anchor points. The DMFI illustrations are consistent with previously published dynamo mechanisms, and allow further investigation of spatially and temporally complex systems. We highlight three types of magnetic structures: (i) magnetic cyclones and (ii) magnetic anticyclones are expelled by, but corotate with axial flow vortices; (iii) magnetic upwellings are amplified by stretching and advection within flow upwellings, and show structural similarity with helical plumes found in rotating hydrodynamic experiments. While magnetic anticyclones are responsible for the regeneration of a stable axial dipole, here we show that excursions and reversals of the dipole axis are caused by the emergence of magnetic upwellings, which amplify and transport a generally multipolar magnetic field from the inner to the outer boundary of the models. Geomagnetic observations suggest the presence of magnetic structures similar to those found in our models; thus, we discuss how our results may pertain to Earth's core dynamo processes. In order to make DMFI a standard tool for numerical dynamo studies, a public software package is available upon request to the authors (supplementary material is available at: http://www.ipgp.jussieu.fr/~aubert/DMFI.html).

Key words: Dynamo: theories and simulations; Geomagnetic excursions; Geomagnetic induction; Reversals: process, timescale, magnetostratigraphy.

1 INTRODUCTION

The theoretical understanding of the geodynamo has been deeply influenced by Alfvén's frozen flux theorem (Alfvén 1943), which states that in a perfectly conducting fluid, magnetic field lines move with the medium, as if they were material lines frozen into it. In the wake of Alfvén's theorem, and before the availability of numerical dynamos, conceptual models (such as the Zeldovitch and Alfvén rope dynamos, for a review see Fearn *et al.* 1988) have been proposed to explain how, following frozen-flux theory, fluid motion could regenerate a pre-existing magnetic field, through the stretching, twisting and folding of magnetic field lines. In the Earth's liquid iron core, the dynamo process occurs in a highly, but not infinitely conducting fluid, where a frozen-flux approximation can be applied within certain limitations: Alfvén's theorem is considered as valid for larger length scales and timescales shorter than, say, a century (Roberts & Scott 1965; Roberts & Glatzmaier 2000).

Since the advent of numerical dynamos, a major goal is to understand their working mechanisms, and the frozen-flux approximation has proven to be a useful theoretical concept, providing a framework for the explanation of geomagnetic observations in terms of field line dynamics (e.g. Olson *et al.* 1999). Although the progress of computer graphics has permitted easier imaging of field lines, three major difficulties still remain: first, the limited applicability of the frozen-flux concept in a finitely conducting fluid complicates the interpretation. Fortunately, the magnetic Reynolds number, which measures the importance of magnetic diffusion in the dynamo process, is of comparable magnitude in Earth and in many dynamo simulations, $Re_m \approx$ 500–1000 (e.g. Christensen & Tilgner 2004). The frozen-flux approximation is, therefore, expected to fail to a similar extent in numerical models and in the core. Magnetic field lines should, therefore, not only move with the fluid, but also diffuse due to Ohmic dissipation, adding another degree of complexity. Second, we face the problem of selecting the right field lines (through a choice of anchor points) that illustrate the relevant features of the dynamo process. If we depict too many lines the result will tend to resemble a 'bowl of spaghetti', blurring the interesting dynamic processes rather than highlighting them. Ideally, we concentrate on just a few field lines that happen to pass through the dynamically meaningful regions. Third, in a time-dependent system the time evolution

Table 1. Set of numerical models, and estimated parameters for the Earth's core. The magnetic Reynolds number Re_m and relative dipole strength f_{dip} are defined as in Christensen & Aubert (2006): $Re_m = UD/\lambda$, where U is the time average, root-mean-squared velocity in the shell, and f_{dip} is evaluated at the outer boundary of the shell as the time average, root-mean-squared amplitude of the dipole relative to the total magnetic field. Earth's core estimates are obtained from Jackson *et al.* (2000), Christensen & Tilgner (2004) and Christensen & Aubert (2006). The Prandtl number in the Earth's core can be either of order 10^{-2} (thermal convection) or much larger than one (chemical convection).

System	Driving	Ra^*	E	Pm	Pr	Re_m	Reversals?	f_{dip}(stable)
C	Chemical	3	3×10^{-4}	3	1	514	Yes	0.23
T	Thermal	7	2×10^{-2}	10	1	110	Yes	0.35
Earth's core	Thermochemical	$\approx 10^{-5}$	$\approx 10^{-14}$	$\approx 10^{-6}$	?	≈ 1000	Yes	0.64 (in 1990)

of the anchor points has to be specified, in a way that ensures that the lines are being followed through time. The frozen-flux approximation requires us to follow material particles, but we risk missing effects related to Ohmic dissipation.

In this paper, we introduce the Dynamical Magnetic Field line Imaging technique (DMFI), which has been developed to represent the time evolution of relevant magnetic field lines in numerical dynamos, and thus provides visual support to the interpretation of their dynamics. The technique is not dependent on the applicability of the frozen-flux approximation, and allows us to image field line creation and dissipation, in addition to events related with advection and deformation. We first identify magnetic structures and highlight their relations with flow structures. This provides a visual confirmation of several previously published dynamo mechanisms. DMFI animations of Earth-like numerical dynamos are then used to highlight, for the first time, the field line mechanism of simulated polarity excursions and reversals.

2 MODELS AND TOOLS

2.1 Numerical models

We consider an electrically conducting, incompressible fluid in a spherical shell of aspect ratio 0.35, rotating about an axis $\mathbf{e}_z$ with constant angular velocity Ω. We solve the magnetic induction equation for the magnetic field $\mathbf{B}$ in the MHD approximation, the Navier–Stokes and thermo-chemical transport equations for the velocity field $\mathbf{u}$ and codensity C (which expresses the density anomaly resulting from a superadiabatic temperature, or excess concentration in light elements) in the Boussinesq approximation. The mechanical boundary conditions are of rigid type. The outer boundary is electrically insulating, while the inner boundary can be either conducting (in model T, see Table 1) or insulating (in model C). The influence of a change in the latter boundary condition is generally thought to be insignificant for Earth's core geometry (Wicht 2002). Our equation system is identical to that given in Christensen & Aubert (2006), except for the use of a codensity formulation for the Boussinesq buoyancy (Braginsky & Roberts 1995; Kutzner & Christensen 2002). The codensity C describes the combined effects of thermal and chemical buoyancies and follows a standard transport equation

$$\frac{\partial C}{\partial t} + \mathbf{u} \cdot \nabla C = \kappa \nabla^2 C + \beta. \tag{1}$$

Here the thermal and chemical diffusivities are assumed to have the same value κ, representing the effects of the turbulent mixing that acts on the temperature and chemical concentration fields. The term β arises in the Boussinesq approximation to describe the cooling of the reference adiabatic thermal state, the non-zero divergence of
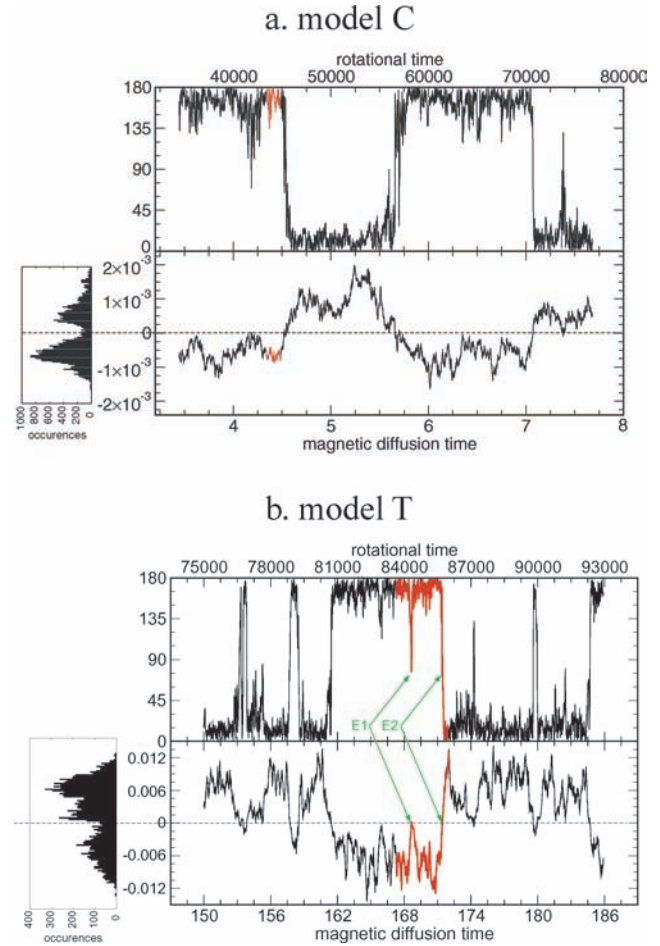

Figure 1. Dipole colatitude in degrees (upper panels), and g_1^0 axial dipole Gauss coefficient of the magnetic potential at the outer boundary (lower panels) as a function of time, for (a) model C and (b) model T. Histograms of the g_1^0 distribution are shown on the left-hand side. The red curves represent the time intervals imaged by DMFI in movies 1 (C) and 2 (T). Time is given in both units of the rotational time $1/\Omega$ (upper axis) and the magnetic diffusion time D^2/η (lower axis). The axial dipole gauss coefficient is given in units of $(\rho\mu)^{1/2}\Omega D$, where ρ and μ are, respectively, the fluid density and magnetic permeability.

the adiabatic thermal gradient, and the enrichment in light elements of the reference chemical state. We choose an end-member thermal model by setting $\beta = 0$ for simplicity, and using a constant temperature difference ΔT between the inner and outer boundary. For an end-member chemical model, we choose a negative uniform β, and adopt a fixed codensity at the inner boundary, and zero codensity flux at the outer boundary. The dimensionless control parameters of the

2 iterations of DMFI algorithm

Highest energy point at time t
used as
anchor point for time t+dt

Highest energy point at time t+dt
used as
anchor point for time t+2dt

Fieldline at time t

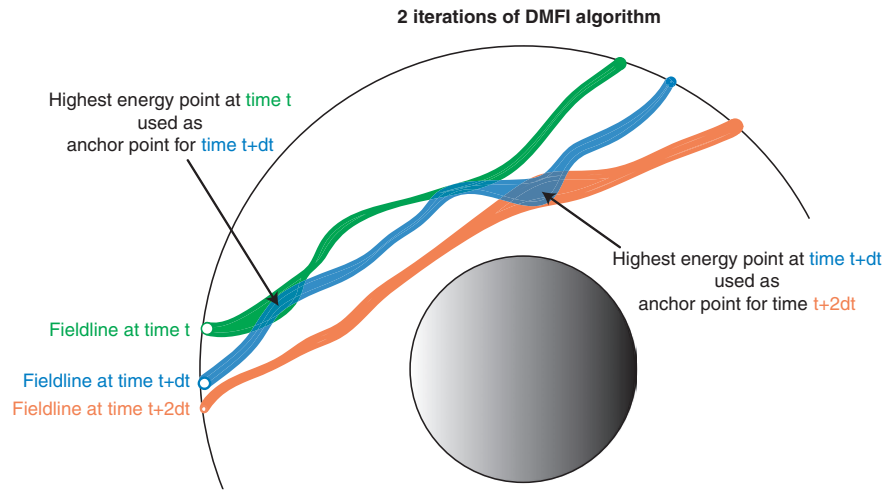Fieldline at time t+dt

Fieldline at time t+2dt

Figure 2. Sketch of the DMFI time-stepping algorithm used to choose dynamically evolving anchor points for the magnetic field lines. The algorithm is initialized with anchor points sampling the radial magnetic field patches at the external boundary of the shell. Subsequently, the anchors are floating and follow the points of maximum magnetic energy along each line (i.e. the points where the lines are thickest in DMFI representation).

system are the Ekman number $E = \nu/\Omega D^2$, Prandtl number $Pr = \nu/\kappa$, magnetic Prandtl number $Pm = \nu/\lambda$, and the Rayleigh number, which is given by $Ra^* = \alpha g_o \Delta T / \Omega^2 D$ and $Ra^* = g_o |\beta| / \Omega^3 D$ for thermal and chemical models, respectively. Here D is the spherical shell gap, g_o is the gravity at the outer boundary of the shell, α is the thermal expansion coefficient, ν and λ are, respectively, the viscous and magnetic diffusivities of the fluid. We use the new PARODY numerical implementation of the equations, written by Emmanuel Dormy and Julien Aubert. PARODY uses a spherical harmonics decomposition in the lateral direction, and a second-order finite differencing scheme in the radial direction, which makes it suitable for parallel computation on distributed memory clusters. PARODY has been benchmarked against other major implementations (Christensen *et al.* 2001).

Table 1 presents the input and output parameters of the models which we have analysed in this study, as well as values inferred for Earth's core conditions. Numerical models operate in a parameter range which is very remote from that of natural objects. As a result, the flow is much too viscous and short-timescale, small-scale phenomena are not simulated. Yet the structure of large-scale (more than 1000 km) and long-timescale (centennial to millennial) flow shows similarities with what is expected from the flow in the Earth's core (e.g. Amit & Olson 2006; Aubert *et al.* 2007), and, due to the relatively small value of the magnetic Reynolds number (which, incidentally, can be reached with numerical models), the magnetic induction should not feel the smaller flow scales (Christensen & Tilgner 2004). A comparison between the output of numerical models and the geomagnetic observations should, therefore, be limited to larger scales and longer timescales.

Time-series of the magnetic dipole tilt and axial dipole component are reported in Fig. 1. The control parameters in models C and T have been selected in the literature (respectively from Kutzner & Christensen 2002; Wicht 2005) for the similarity of some of the model outputs with what is known of the geomagnetic and palaeomagnetic field: a reasonably Earth-like magnetic Reynolds number Re_m (see Table 1 for definition) and the existence of well-defined stable and reversing polarity phases. More quantitatively, this corresponds to the existence of a bi-modal histogram of the g_1^0 axial dipole Gauss coefficient of the CMB magnetic potential (Valet &

Meynadier 1993). As one increases the convective forcing, the onset of reversals is usually close to the point where the dipole part of the generated magnetic field ceases to dominate the magnetic spectrum (Olson & Christensen 2006). Within the parameter range currently accessible to numerical dynamos, it is, therefore, difficult to obtain reversals while maintaining a significant relative dipole strength f_{dip} during stable polarity phases, as observed for the Earth's core.

2.2 Outline of DMFI visualization

The DMFI algorithm relies on 15 floating anchor points seeded inside the fluid shell. The anchor points are not used as terminations of field lines. Rather, from each point we draw the field line corresponding to the magnetic field **B**, and that corresponding to the magnetic field −**B**. Using this method, we are able to draw field lines through our floating anchors, which terminate as they reach the outer boundary of the spherical shell (the outside potential field is not depicted). The field lines are rendered as tubes with a thickness which is proportional to the local magnetic energy **B**^{2} (Fig. 3a). Such a representation naturally depicts the most energetic field lines in the fluid interior and, thus, assigns less visual impact to lines which carry little magnetic energy.

Fig. 2 is a sketch of the time-stepping algorithm for floating anchor points: After rendering field lines at time t, the algorithm searches for the point of maximum magnetic energy along each line (the point where the line is thickest), and selects it as the new anchor point for time $t + dt$. This ensures representation of the most energetic magnetic field structures. We have performed a simple test of the relevance of DMFI in Fig. 3(b). An isosurface of the magnetic energy has been represented at a level of 10 per cent of the maximal magnetic energy, which is also approximately eight times the mean magnetic energy. This isosurface encloses 25 per cent of the total energy in the shell, in 1.6 per cent of the shell volume. The magnetic energy distribution in the shell is volumetrically quite sparse, as previously noted by Kageyama & Sato (1997), and, thus, is accurately represented through the field lines chosen by the DMFI algorithm.

Our models C and T have been visualized using DMFI, and the results are presented in the supplementary movies 1 and 2 of this paper. The DMFI-imaged time intervals are marked in red in Fig. 1.
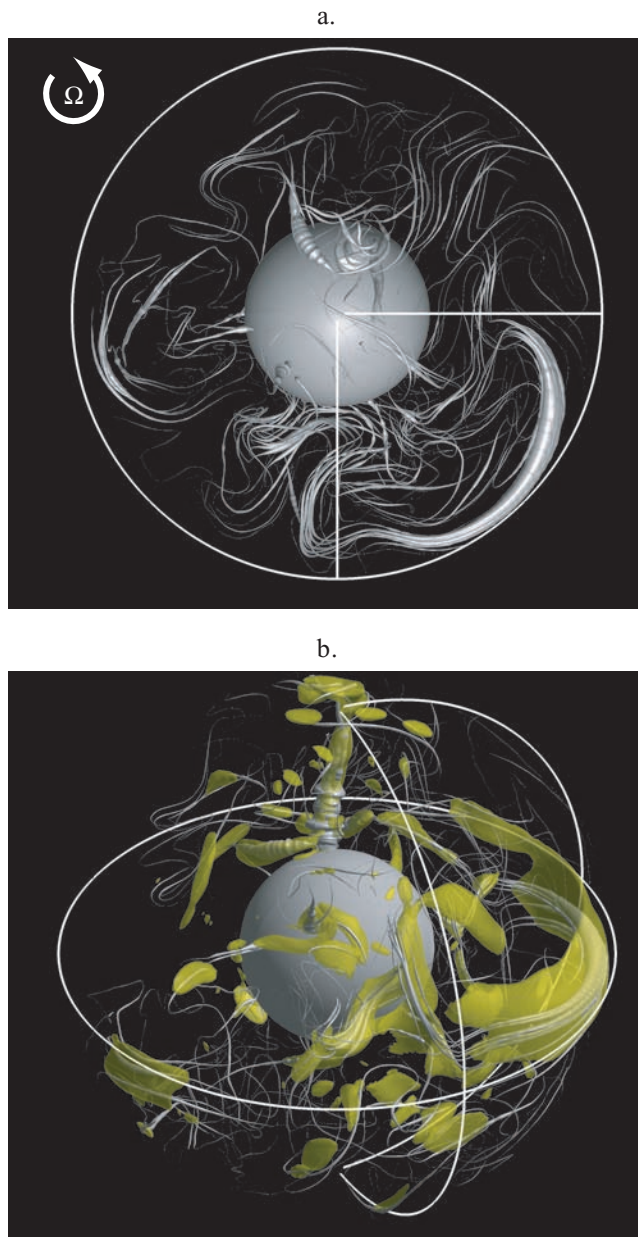
a.

b.

Figure 3. (a) Top view (the $\mathbf{e}_z$ vector is pointing towards the reader) of a DMFI snapshot in model C, at magnetic diffusion time 4.36078. Magnetic field lines are rendered with a thickness proportional to $\mathbf{B}^2$. Two meridians (at $\varphi = 0°$ and $\varphi = 270°$) and the equator are drawn in white. (b) Side view of same model. A magnetic energy isosurface (yellow) is drawn at 10 per cent of the maximal value, enclosing 25 per cent of the total magnetic energy in 1.6 per cent of the shell volume.

3 RESULTS

3.1 Magnetic structures and time-dependent dynamo mechanisms

In this section, we examine the mechanisms governing the time evolution of magnetic field lines. The magnetic Reynolds number Re_m measures the relative importance of creation and advection with respect to diffusion and should be as Earth-like as possible for geophysical relevance. We therefore, choose to study model C in detail. This model is however quite intricate due to the small-
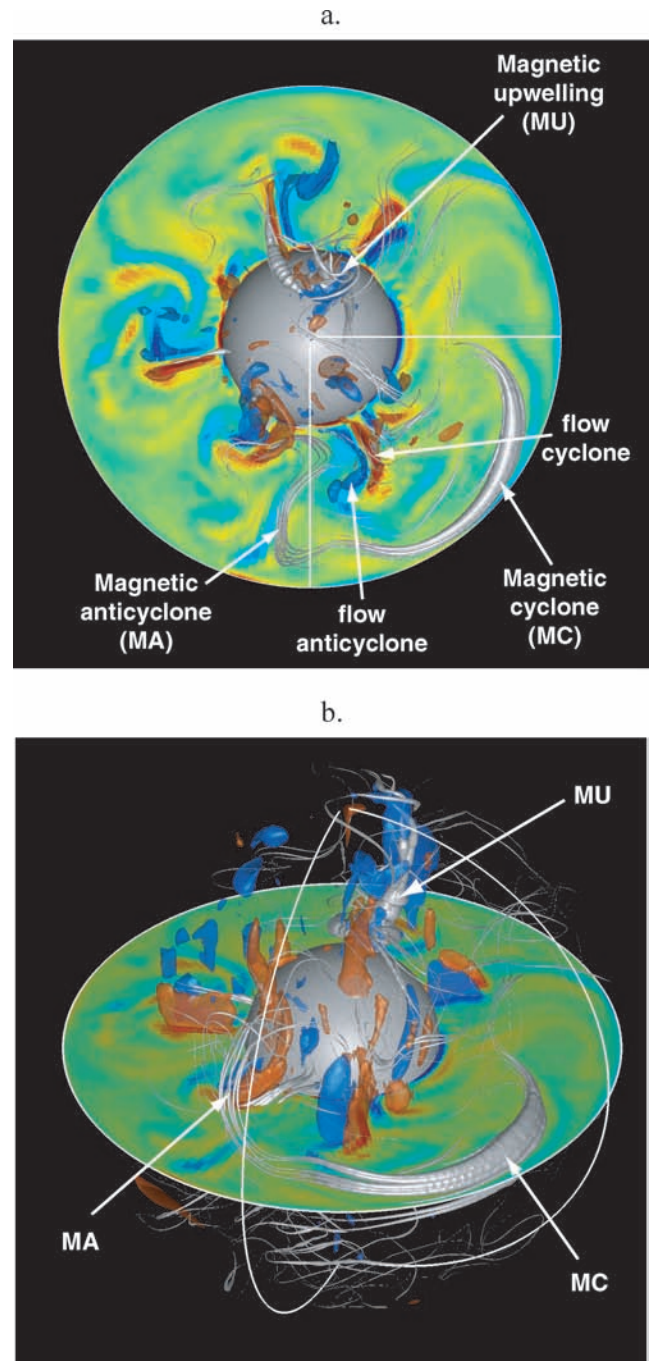
a.

b.

Figure 4. Top (a) and side (b) views of DMFI field lines in model C at magnetic diffusion time 4.36078, with same conventions as in Fig. 3. The equatorial plane is colour-coded with the axial vorticity $\omega_z = \boldsymbol{\omega} \cdot \mathbf{e}_z$ (colour map from -3, blue to +3, red, in units of Ω). Two volume isosurfaces of ω_z are represented at levels -1.5 (blue) and 1.5 (red).

scale character of magnetic structures and weak dipolarity. We therefore also use model T, which has larger scale structures and a more dipolar field morphology, to illustrate some aspects of the dynamo process. Note, however, that model T has a significantly lower Re_m.

Fig. 4 shows a coupled visualization of DMFI field lines and flow vortices, represented through the axial component $\omega_z = \boldsymbol{\omega} \cdot \mathbf{e}_z$ of the vorticity $\boldsymbol{\omega} = \nabla \times \mathbf{u}$. The Coriolis force organizes the
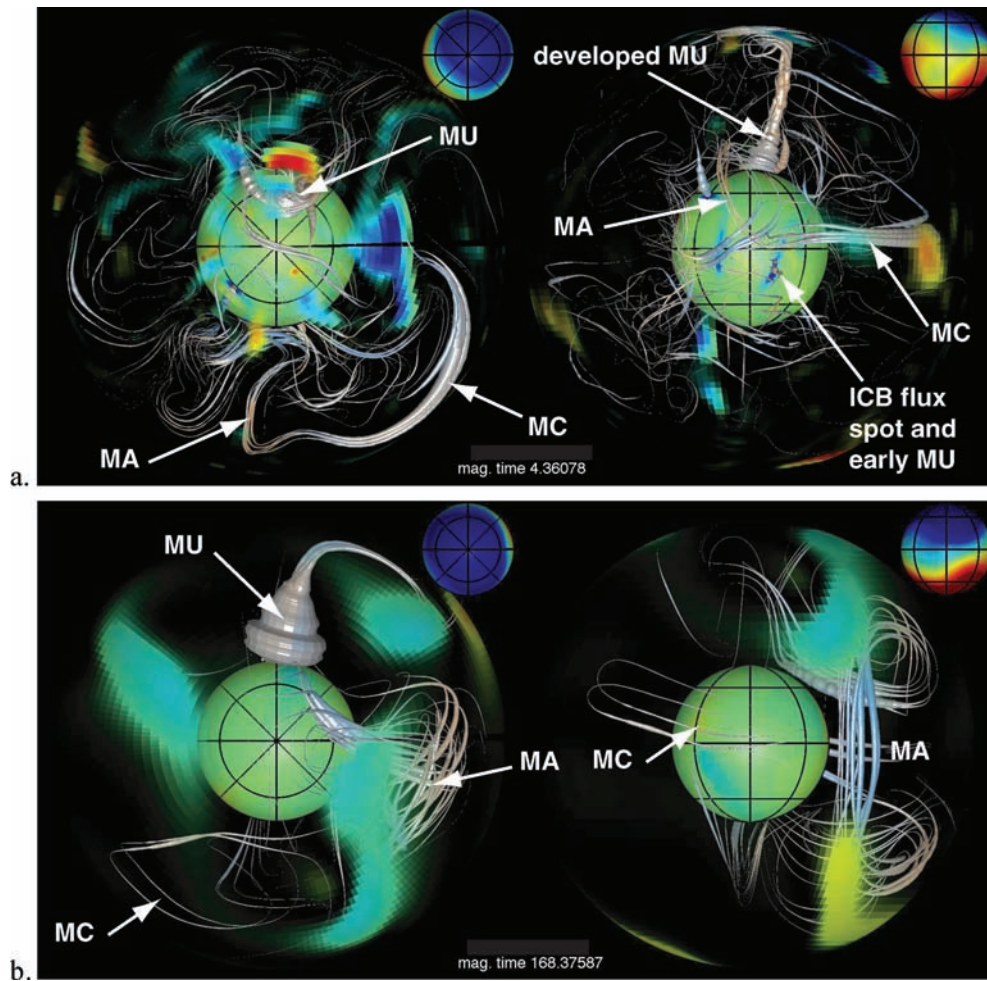
Figure 5. Snapshots from (a): DMFI movie 1 of model C and (b): movie 2 of model T. Left-hand panels: top view. Right-hand panels: side view. The inner (ICB) and outer (CMB) boundaries of the model are colour-coded with the radial magnetic field (a red patch denotes outwards oriented field). In addition, the outer boundary is made selectively transparent, with a transparency level that is inversely proportional to the local radial magnetic field. Field lines are also colour-coded in order to indicate $\mathbf{e}_z$-parallel (red) and antiparallel (blue) direction. The radial magnetic field as seen from the Earth's surface is represented in the upper-right inserts, in order to keep track of the current orientation and strength of the large-scale magnetic dipole. Colour maps for (a): ICB field from -0.12 (blue) to 0.12 (red), in units of $(\rho\mu)^{1/2}\Omega D$, CMB field from -0.03 to 0.03, Earth's surface field from $-2\ 10^{-4}$ to $2\ 10^{-4}$. For (b): ICB field from -0.72 to 0.72, CMB field from -0.36 to 0.36, Earth's surface field from $-1.8\ 10^{-3}$ to $1.8\ 10^{-3}$.

vortices into columns elongated along the $\mathbf{e}_z$ axis of rotation, due to the Proudman–Taylor constraint. The sparse character of the magnetic energy distribution results from the tendency of field lines to cluster at the edges of flow vortices due to magnetic field expulsion (Weiss 1966; Galloway & Weiss 1981). Since magnetic field lines correlate well with the flow structures in our models, we will subsequently visualize the magnetic field structure alone. The supporting movies of this paper (see Fig. 1 for time window and Figs 5–9 for extracts) present DMFI field lines, together with radial magnetic flux patches at the inner boundary (which we will refer to as ICB) and the selectively transparent outer boundary (CMB). We will first introduce the concept of a magnetic vortex, which is defined as a field line structure resulting from the interaction with a flow vortex. By providing illustrations of magnetic cyclones and anticyclones, DMFI provides a dynamic, field-line based visual confirmation of previously published dynamo mechanisms (Kageyama & Sato 1997; Olson *et al.* 1999; Sakuraba & Kono 1999; Ishihara & Kida 2002), and allows the extension of such descriptions to time-dependent, spatially complex dynamo regimes.

3.1.1 Magnetic cyclones

A strong axial flow cyclone (red isosurface in Fig. 4) winds and stretches field lines to form a magnetic cyclone. Fig. 6 relates DMFI visualizations of magnetic cyclones, as displayed in Figs 4 and 5, with a schematic view inspired by Olson *et al.* (1999). A magnetic cyclone can be identified by the anticlockwise motion of field lines clustered close to the equator, moving jointly with fairly stable high-latitude CMB flux patches concentrated above and below the centre of the field line cluster. Model C (movie 1, Fig. 5a) exhibits very large-scale magnetic cyclones (times 4.3617, 4.3811), which suggest an axial vorticity distribution biased towards flow cyclones. Inside these vortices, the uneven distribution of buoyancy along $\mathbf{e}_z$ creates a thermal wind secondary circulation (Olson *et al.* 1999), which is represented in red on Fig. 6. This secondary circulation concentrates CMB flux at high latitudes, giving rise to relatively long-lived (several vortex turnovers) flux patches similar to those found in geomagnetic field models. Simultaneously, close to the equatorial plane, the secondary circulation concentrates field lines into bundles and also pushes them towards the outer boundary, where
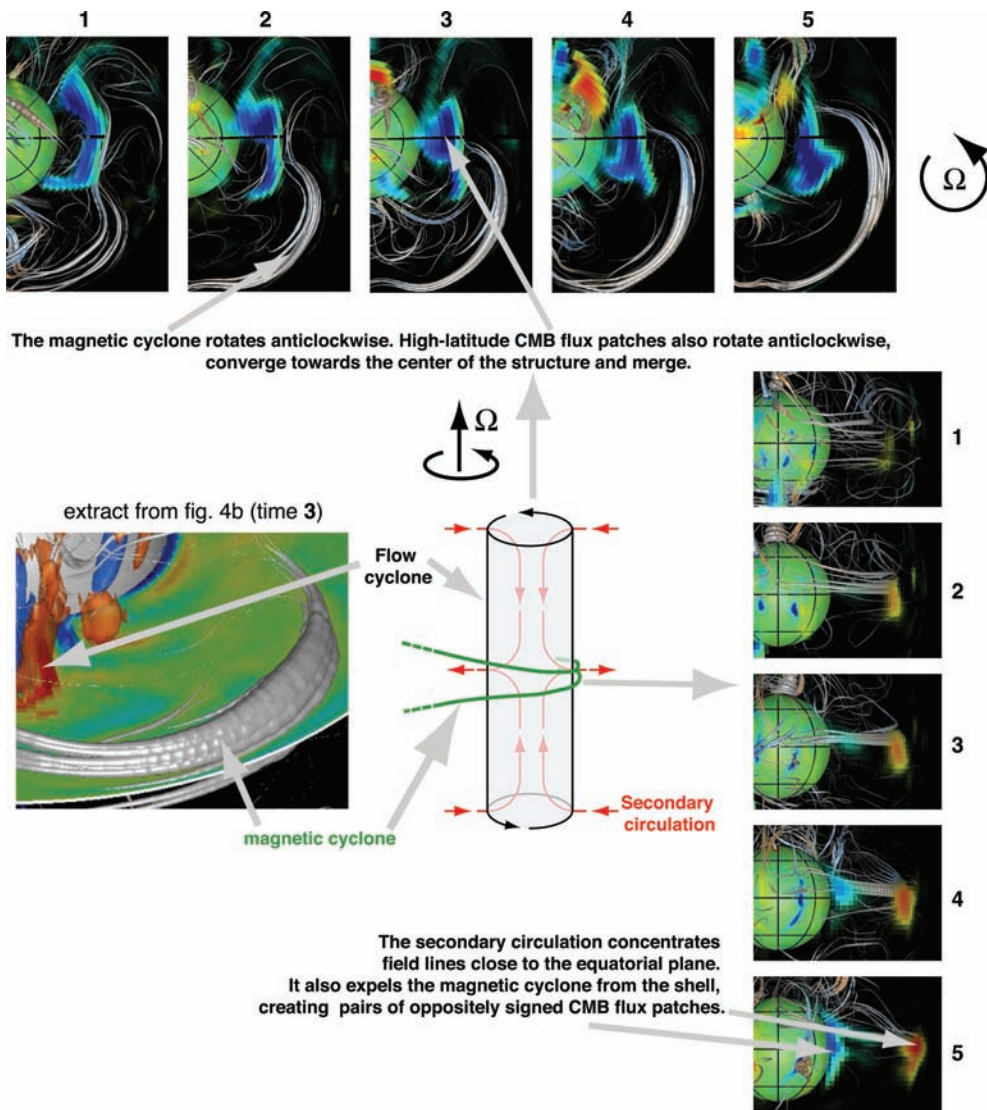
Figure 6. Schematic description of the generation of a magnetic cyclone, together with DMFI extracts from movie 1 (model C). The sequence snapshots 1–5 are taken from times 4.35982, 4.36030, 4.36078, 4.36127, 4.36187.

they are ultimately expelled from the shell, creating pairs of CMB patches with oppositely signed flux in a kinematic mechanism similar to that envisaged by Bloxham (1986). These low-latitude CMB flux features are rather short-lived (typically a vortex turnover) because there is no flow producing a dynamo cycle to sustain them; their decay involves significant Ohmic dissipation, in violation of the frozen-flux theorem.

3.1.2 Magnetic anticyclones

The magnetic anticyclones, which result from the magnetic field interaction with axial flow anticyclones (blue isosurfaces in Fig. 4) can be recognized through their characteristic shape illustrated on Fig. 7, underlying an alpha-squared dynamo mechanism (Olson *et al.* 1999). Since model C is biased towards flow cyclones, we rather use model T (movie 2 at time 168.375, Figs 5b and 7), for a clearer picture. An initial poloidal field is first wound by the anticyclone in the azimuthal (toroidal) direction. Flow anticyclones have the opposite secondary circulation to flow cyclones. The northern and southern toroidal parts of the line are, therefore, stretched away from the equatorial plane as the line winds into the anticyclone.

This stretching regenerates a poloidal field line with the same polarity as the initial line. The flux from the newly generated poloidal field lines reaches the outer boundary, creating high-latitude CMB flux patches of normal polarity above and below the magnetic anticyclone. These patches are usually short-lived (less than a vortex turnover), because they are pushed away by a secondary circulation which has the exact opposite effect to that of magnetic cyclones.

3.1.3 Magnetic upwellings

Among the most remarkable structures highlighted by DMFI sequences, we define magnetic upwellings as energetic field lines generated within buoyancy-driven flow upwellings. These have previously received much less attention than magnetic vortices: their existence has been previously suspected from the analysis of poloidal field line dynamics during reversals (Wicht & Olson 2004), or through the appearance of tangent cylinder CMB flux patches closely related to helical flow upwelling plumes (Sreenivasan & Jones 2006). Here we provide the first description of their structure and dynamics. Models C and T show intermittent magnetic upwellings, either inside (Figs 5a and 8, times 4.3609, 4.4696 in movie
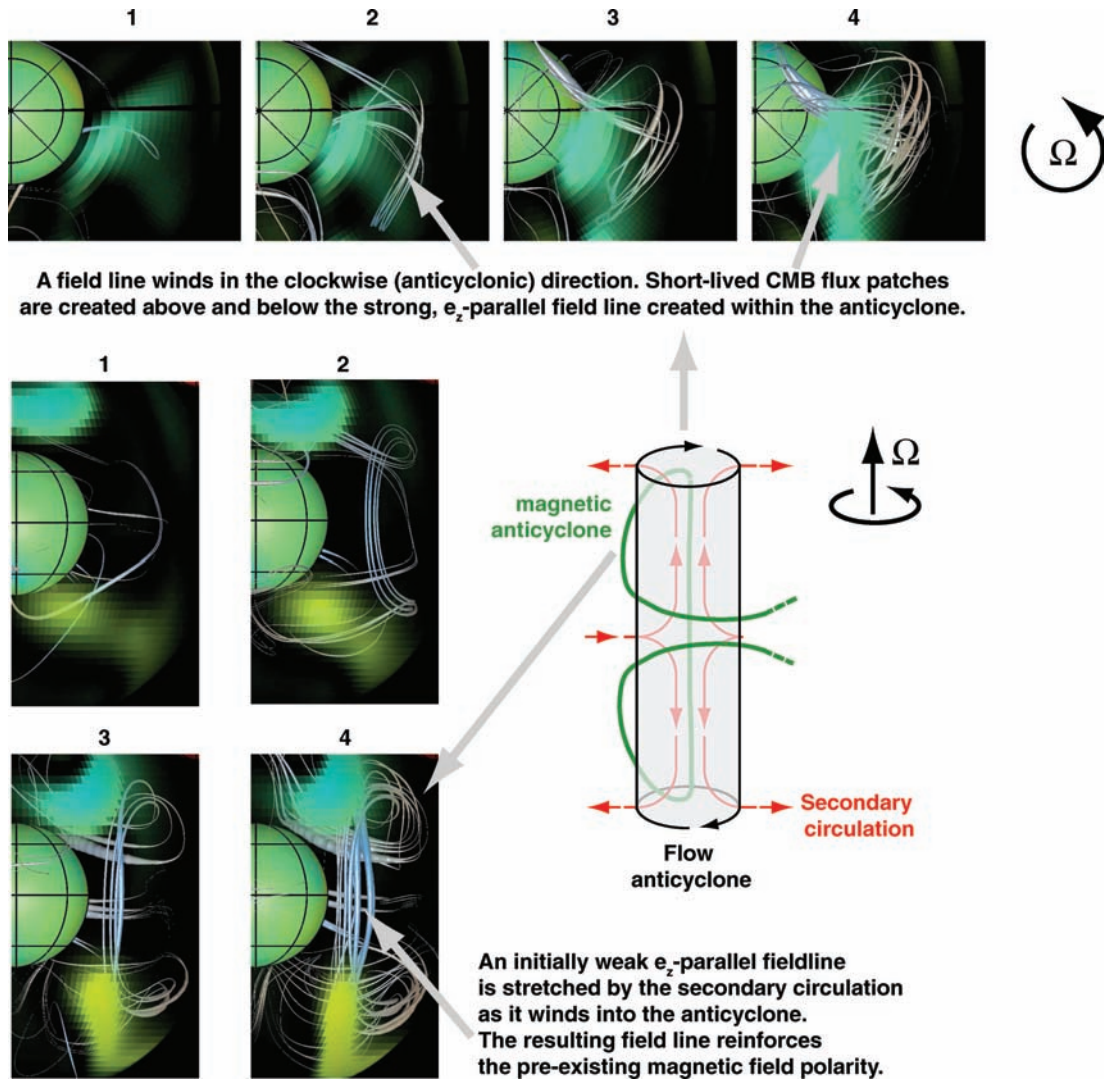
Figure 7. Schematic description of the generation of a magnetic anticyclone, together with DMFI extracts from movie 2 (model T). The sequence snapshots 1–4 are taken from times 168.366, 168.369, 168.373 and 168.376.

1) or outside the tangent cylinder (Figs 5b and 9, time 4.3575 in movie 1, 171.306 in movie 2). Inside the tangent cylinder, they are mostly parallel to, but not necessarily colinear with $\mathbf{e}_z$. Outside the tangent cylinder, they are mostly parallel to the cylindrical radial direction, and are found close to the equatorial plane.

Fig. 8 schematically describes our model mechanism for the creation of a polar magnetic upwelling. Thermal wind-driven plumes reside within the tangent cylinder (Aurnou *et al.* 2003; Aubert 2005). At the base of these upwellings, a converging flow concentrates the ICB magnetic flux into intense spots, which seed the magnetic field growth. The magnetic stretching $(\mathbf{B} \cdot \mathbf{e}_z)\partial(\mathbf{u} \cdot \mathbf{e}_z)/\partial z$ (which is part of the induction term in the magnetohydrodynamic induction equation) is responsible for the magnetic field amplification close to the ICB. The magnetic field line is subsequently advected towards the CMB, where the negative $\partial(\mathbf{u} \cdot \mathbf{e}_z)/\partial z$ de-amplifies the magnetic field. As a result, only a small part of the field $\mathbf{B}$ from the magnetic upwelling directly exits across the CMB. However, the stretching $\partial(\mathbf{u} \cdot \mathbf{e}_z)/\partial z$ also acts on the ambient vorticity field $2\mathbf{\Omega}$ to create anticyclonic helical flow, inducing a strong magnetic field $\mathbf{B}$ (Fig. 8a). When the helical plume axis is nearly colinear with the rotation axis, then $\mathbf{B}$ is purely azimuthal. In this situation, none of the in-

duced magnetic flux should exit across the CMB. This can explain why CMB flux patches are not observed above magnetic upwellings which are aligned closely with the rotation axis (for instance in movie 1 at time 4.4706). However, strong CMB patches often arise while the helical plumes are migrating in cylindrical radius (Fig. 8, DMFI snapshot 3), when their axes are bending away from the axial direction (snapshot 4), or when they are unravelling (snapshot 5). Away from the rotation axis, the tops of the helical plumes efficiently push induced azimuthal flux across the CMB on the side of the plume at larger cylindrical radius, as shown schematically in Figs 8(b) and (c). This model predicts that high latitude flux patches will occur in oppositely signed pairs. However, qualitative review of the DMFI sequences (see Fig. 8) suggests that a bias may exist towards the polarity carried by the underlying magnetic upwelling. We hypothesize that some of the ambient field $\mathbf{B}$ reaches the CMB, in addition to the induced field due to the upwelling, $\mathbf{B}$. This may be due to an asymmetric effect of the positive (amplifying) and negative (de-amplifying) upwelling along the upwelling path, or to the effect of magnetic diffusion.

Equatorial magnetic upwellings (Fig. 9) are created close to the equatorial part of the ICB, where the concentrated magnetic flux
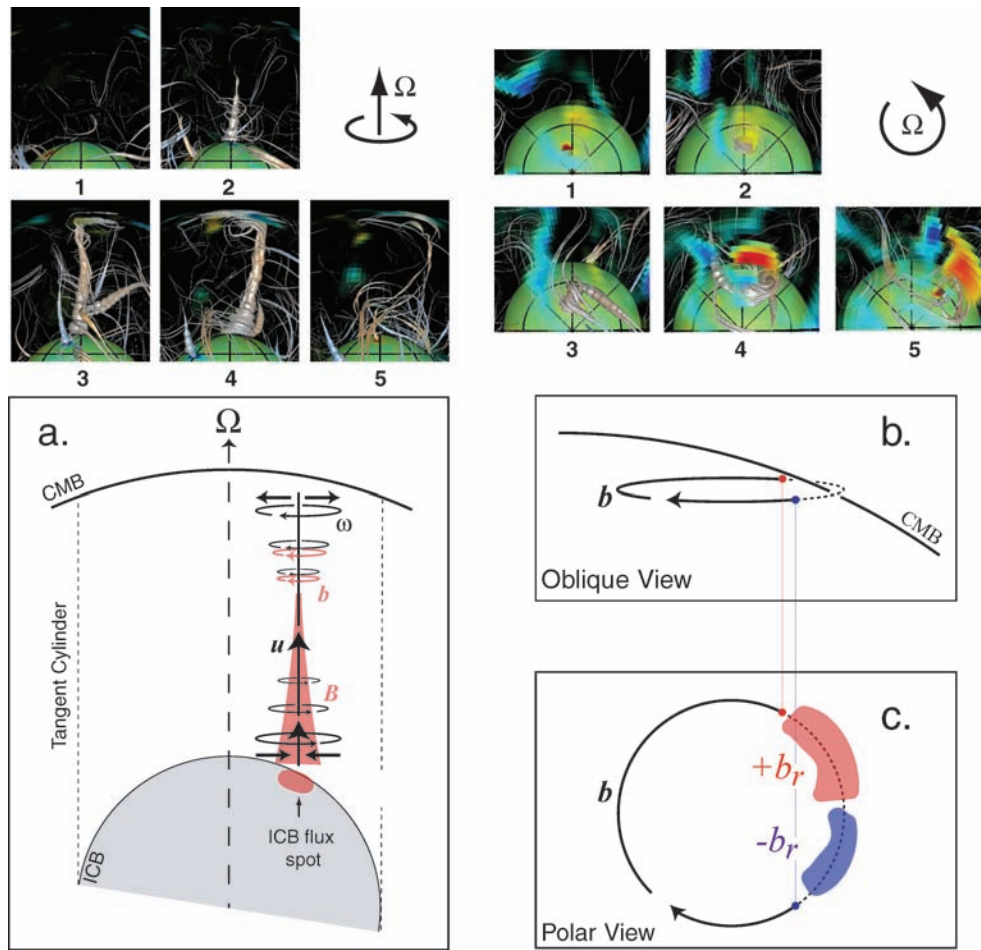
Figure 8. Mechanism for the generation of polar magnetic upwellings, together with DMFI images of model C (times 1–5, respectively, correspond to magnetic diffusion times 4.3584, 4.3589, 4.3598, 4.3608 and 4.3613). (a) Schematic side view of a polar magnetic upwelling. The converging flow beneath ICB upwellings concentrates magnetic flux patches into intense spots seeding the magnetic field growth. Stretching and advection inside the upwellings subsequently amplify the magnetic field bundle which rises in the $\mathbf{e_z}$ direction. Magnetic upwellings inside the tangent cylinder rise within helical flow plumes which are not colinear but parallel to the rotation axis. (b) Oblique close-up of the magnetic field induced by the helical flow plume, $\mathbf{b}$, crossing the CMB within the tangent cylinder. (c) Top view of the induced field, $\mathbf{b}$, and associated entering (blue) and exiting (red) CMB flux patches.

patches get near to the quasi-geostrophic columnar flow upwellings residing outside the tangent cylinder. The mechanism for their generation is largely the same as that of polar magnetic upwellings. However, they are not associated with helical flow plumes since the ambient vorticity field $\mathbf{2\Omega}$ is not stretched by cylindrical radial motion. Equatorial upwellings, therefore, lack the magnetic flux expulsion mechanism seen with polar upwellings, and have little to no observable signature at the CMB.

Helical plumes visualized using fluorescein dye (Fig. 10 and movie 3) in laboratory experiments of tangent cylinder convection (Aurnou *et al.* 2003) show a structure similar to that of magnetic upwellings imaged by DMFI in the tangent cylinder (DMFI sequence in Fig. 8). While dye is a passive tracer, the magnetic field should be seen as an active tracer, although Lenz's law predicts that it should minimize the disturbances caused to the flow. Both tracers are injected at the same location (ICB) and advected in a comparable manner by the two systems. This suggests that the flow inside a hydrodynamic helical plume in the experiment is similar to that found in the numerics, although helical plumes are typically more numerous (about 20 in the experiments of Aurnou *et al.* (2003)) when the magnetic field is absent (Sreenivasan & Jones 2005; Sreenivasan & Jones 2006). We note indeed that the vorticity and magnetic fields

are both subject to stretching due to the upwelling $\partial(\mathbf{u} \cdot \mathbf{e_z})/\partial z$. Close to the ICB, stretching the background vorticity field $\mathbf{2\Omega}$ and ambient magnetic field $\mathbf{B}$ in an upwelling plume [e.g. positive $\partial(\mathbf{u} \cdot \mathbf{e_z})/\partial z$] will both create positive (cyclonic) axial vorticity and amplify $\mathbf{B}$.

3.2 The mechanism of excursions and reversals

In our models, the bi-modal character of the g_1^0 axial dipole component histogram (Fig. 1), which is also present in the geomagnetic time-series (Valet & Meynadier 1993) suggests an attraction of the dynamo system towards a stable dipole either parallel or antiparallel with the axis of rotation. The field line loops found within magnetic anticyclones indeed provide a mechanism through which an existing predominantly axial dipole may be amplified and stabilized. However, the g_1^0 time-series in Fig. 1 also show that this attraction is frequently challenged by events breaking this polarity, leading to excursions and reversals of the dipole axis. These events may be linked to changes in the amplitude and distribution of CMB flux patches, as shown by Olson & Amit (2006) for the geomagnetic field. We now analyse the field line structure underlying these changes.
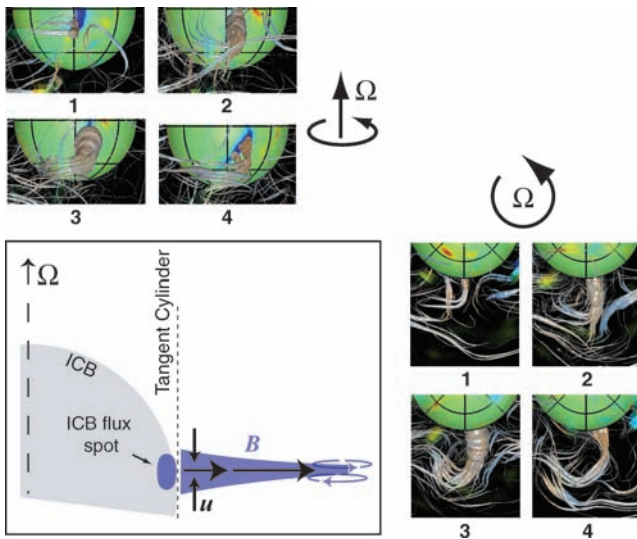
Figure 9. Mechanism for the generation of equatorial magnetic upwellings, together with DMFI images of model C (times 1–4, respectively, correspond to magnetic diffusion times 4.3563, 4.3569, 4.3573 and 4.3585). Same conventions as in Fig. 8.
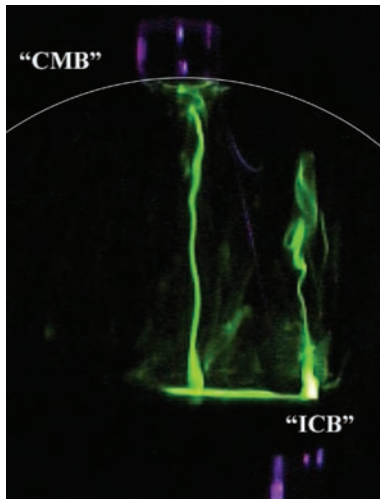

Figure 10. Sideview photograph of helical plumes in laboratory experimental simulations of tangent cylinder convection. Water is the working fluid; fluorescein dye marks the two plumes. Control parameters: flux Rayleigh number $Ra_F = 4.4 \times 10^9$; Ekman number $E = 4.3 \times 10^{-5}$, corresponding to a rotation period of $T = 7.0$ s, Prandtl number $Pr = 7$. Also, see supporting movie 3, made using a digital video camera in the rotating frame, which shows the formation and evolution of the helical plumes shown in this image over approximately 10 rotation periods. Further experimental details can be found in Aurnou *et al.* (2003).

The ICB magnetic field of our models generally has a much weaker axial dipole component than the CMB field (movies 1–2 and Fig. 5). Indeed the magnetic flux threading the ICB is influenced by chaotic concentration and mixing, while the CMB flux is ordered by magnetic anticyclones. The central observation brought by DMFI is that a polarity breaking event occurs when the ICB multipolar field is amplified and brought to the CMB by a coherent set of magnetic upwelling field lines. To illustrate this, we use model T which has a large-scale magnetic structure. Movie 2 contains two major polarity breaking events, both of which coincide with a large decrease of $|g_1^0|$ in Fig. 1. Event E1 occurs at magnetic diffusion time
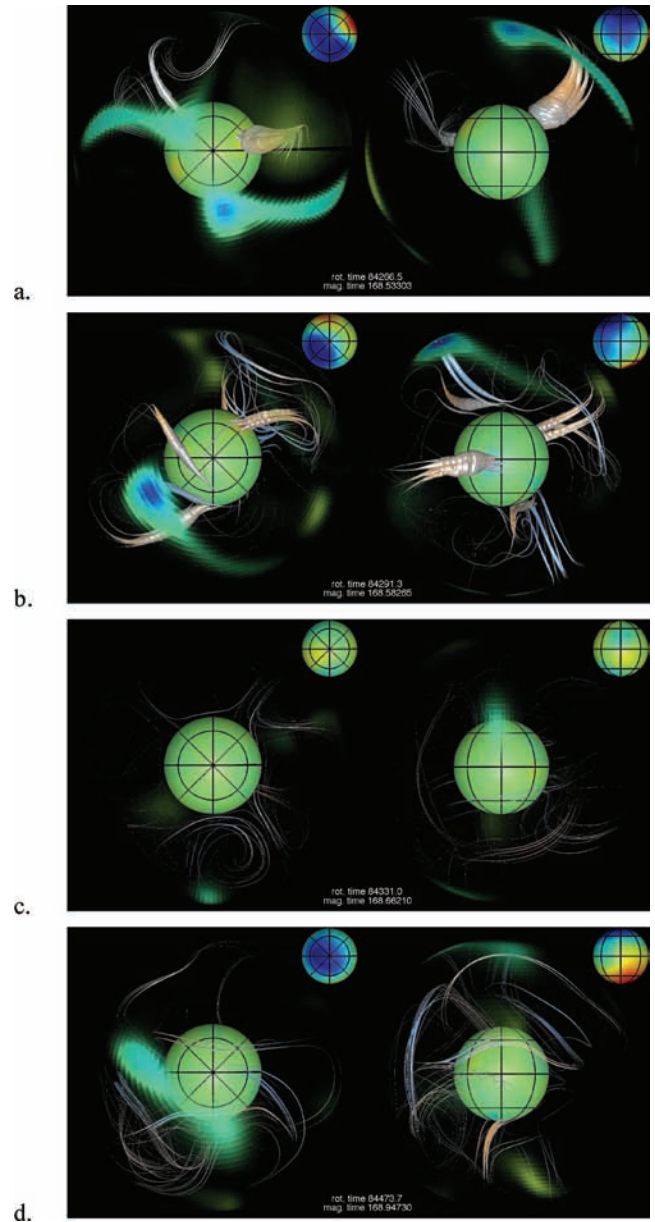

Figure 11. The steps involved in event E1, an excursion of the dipole axis occurring at time 168.52 in movie 2 (model T).

168.52 and leads to an excursion of the dipole axis. Event E2 occurs at time 171.32 and leads to a full reversal. The successive steps of these events are imaged in Figs 11 and 12. In movie 2, as well as Figs 11–12, the upper-right inserts indicate the magnetic field as it would be seen from the surface of the Earth. Moreover, the colour-coding of the field lines is important as it hints for their direction: field lines are red-tinted when directed upwards ($\mathbf{e}_z$-parallel), and blue-tinted when directed downwards ($\mathbf{e}_z$-antiparallel).

Event E1 starts with the rise of a magnetic upwelling in the northern hemisphere, within the tangent cylinder (Fig. 11a). Growing from an inverse (red) ICB flux spot, this structure has inverse polarity, and some of its flux exits at the CMB. The occurrence of this magnetic upwelling enriches the magnetic field inside the shell with an equatorial dipole component, which is then further amplified by equatorial magnetic upwellings (Fig. 11b). At time 168.583, the field lines of the original axial dipole (blue) co-exist with predominantly
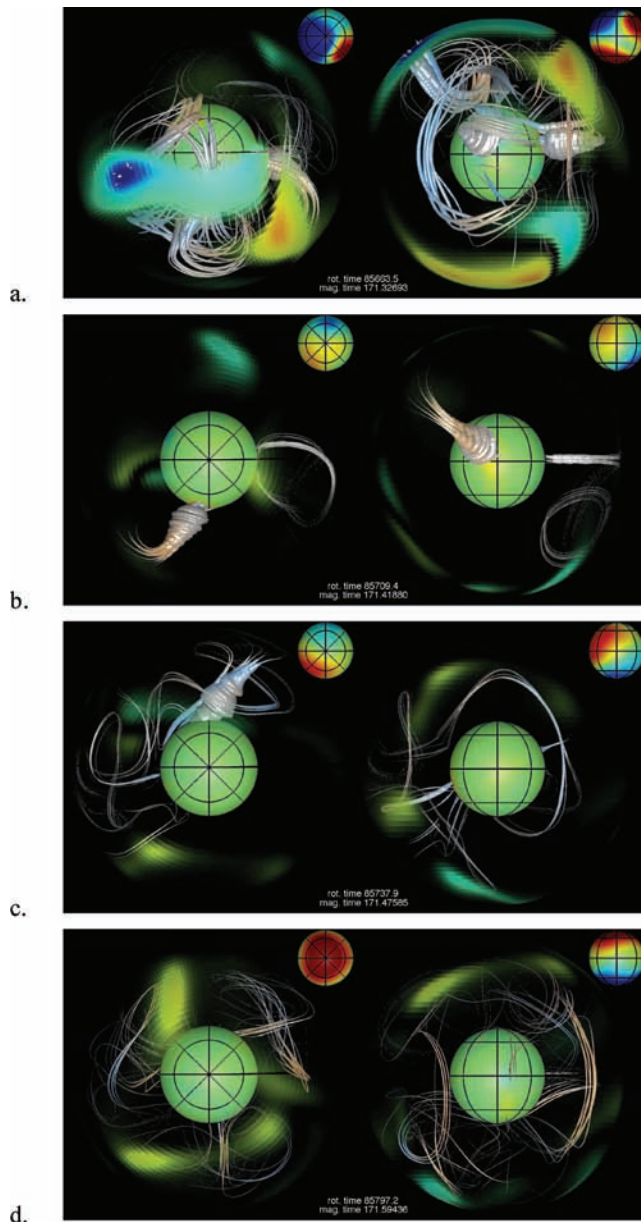
Figure 12. The steps involved in event E2, a full reversal of the dipole axis occurring at time 171.32 in movie 2 (model T).

equatorial field lines of inverse (red) polarity. In this context, faint magnetic anticyclones producing poloidal field lines of both polarities can be observed, which do not have a net effect on the regeneration of the axial dipole, which in turn collapses. The equatorial dipole component is also bound to collapse due to the intermittent character of the upwellings which maintain it. A low amplitude multipolar state, therefore, takes place in the whole shell, where again faint magnetic anticyclones of both polarities can be seen at different locations (Fig. 11c). After time 168.71 the normal polarity (blue) magnetic anticyclones take precedence, and regenerate an axial dipole in 0.2 magnetic diffusion times (Fig. 11d).

Event E2 starts with two equatorial magnetic upwellings, growing from ICB flux spots of opposite polarity, at the edges of adjacent axial vortices (Fig. 12a). The blue upwelling feeds a normal polarity (blue) magnetic anticyclone, while the red upwelling feeds an inverse polarity (red) magnetic anticyclone. At time 171.327 this com-

petition between normal and inverse structures is felt at the CMB, as well as at the surface, through an axial quadrupole magnetic field. As in event E1, the axial dipole is not efficiently maintained by this configuration, leaving mostly equatorial field lines inside the shell, maintained by two equatorial magnetic upwellings (Fig. 12b), with slightly inverse (red) $\mathbf{e}_z$ orientation. Also similar to event E1, a competition between faint normal and inverse magnetic anticyclones can be observed (Fig. 12c) until time 171.5 where inverse structures take precedence and rebuild an axial dipole (Fig. 12d), thus completing the reversal sequence. The DMFI sequence for event E2 highlights the role of magnetic upwellings in a scenario which is broadly consistent with that proposed by Sarson & Jones (1999).

In the smaller-scale model C, the influence of magnetic upwellings on the dipole latitude and amplitude is not as clear-cut as in model T. Their appearance are, however, associated with tilting of the dipole axis as seen from the Earth's surface (see upper-right inserts in movie 1). Thus, we argue that two essential ingredients for the production of excursions and reversals in numerical dynamos are the existence of magnetic upwellings and a multipolar ICB magnetic field. This agrees with the models of Wicht & Olson (2004), in which the start of a reversal sequence was found to correlate with upwelling events inside the tangent cylinder.

4 DISCUSSION

Understanding the highly complex processes of magnetic field generation in the Earth's core is greatly facilitated by Alfvén's theorem and the frozen-flux approximation, provided one supplies an imaging method which is adapted to the intrinsically 3-D and time-dependent nature of the problem, and also takes into account diffusive effects. The DMFI technique used in the present study aims at achieving this goal, and highlights several magnetic structures: magnetic anticyclones are found outside axial flow anticyclones, and regenerate the axial dipole through the creation of magnetic loops characteristic of an alpha-squared dynamo mechanism. Magnetic cyclones are found outside axial flow cyclones, and concentrate the magnetic flux into bundles where significant Ohmic dissipation takes place. Our description of magnetic vortices confirms and illustrates previously published mechanisms, as presented for instance by Olson *et al.* (1999). By separating the influence of cyclones and anticyclones, we extend these views to more complex cases where there is a broken symmetry between cyclonic and anticyclonic motion. Furthermore, we present the first field line dynamic descriptions of magnetic upwellings, which are created by field line stretching and advection inside flow upwellings.

Our models show that the magnetic structures are robust features found at high (model T) as well as moderately low (model C) values of the Ekman number. This suggests that they pertain to the Earth's core. Since we only have access to the radial component of the magnetic field at the Earth's CMB, our description of the magnetic structure underlying CMB flux patches in the models is of particular interest. Inside the tangent cylinder, short-lived CMB patches of both polarities can be created by the expulsion of azimuthal flux within a magnetic upwelling. These patches are quickly weakened by the diverging flow on the top of the upwelling, therefore, they do not last more than a vortex turnover, which is equivalent to 60–300 yr in the Earth's core (Aubert *et al.* 2007). The observation of a tangent cylinder inverse flux patch in the present geomagnetic field (Olson & Aurnou 1999; Jackson *et al.* 2000; Hulot *et al.* 2002), although it is weakly constrained and not observed with all field regularizations

(Jackson 2003), could support the existence of short-lived magnetic upwellings in the Earth's core.

The origin of the ubiquitous high-latitude flux patches observed outside the tangent cylinder could be attributed to both magnetic anticyclones and cyclones. However, only cyclones can sustain long-lived (several vortex turnovers, centennial to millennial timescales) magnetic flux patches, such as observed in historical geomagnetic field models. In contrast, the sudden appearance of a mid-latitude reversed flux patch, as seen in present-day observations below the southern tip of Africa, could be attributed to a reverse magnetic anticyclone fed by an underlying equatorial magnetic upwelling (which itself does not have a CMB signature).

At low latitudes, magnetic cyclones tend to create oppositely signed pairs of flux patches, while the geomagnetic observations argue more for chains of intense equatorial flux spots of the same polarity (Jackson 2003). While this is an observation that the current generation of numerical models clearly fails to reproduce, we can infer that such an arrangement of flux spots could be caused by a meandering toroidal field line, such as observed for instance in movie 1 at time 4.41450. The meandering is caused by an arrangement of alternating flow cyclones and anticyclones. The expulsion of such a line, over a background poloidal field biased towards one polarity, could cause the observed flux spot chain, as proposed earlier by Finlay (2005).

In this study, we have provided the first field line-based description of the mechanisms of excursions and reversals. As already suggested by Wicht & Olson (2004), little or no dramatic changes in the fluid flow are needed to produce these phenomena: they occur when the multipolar magnetic field present at the ICB is amplified enough, and brought far enough by magnetic upwellings, thus disrupting the production of a normal dipolar field by magnetic vortices. This condition can be quantified by noting that the timescale for upwellings $\tau_U = D/U$ (where U is a typical radial velocity in the fluid) should be smaller than the timescale for the turnover of vortices $\tau_\omega = 1/\omega$ (where ω is a typical fluid vorticity). The ratio of the two timescales is a Rossby number $Ro_l = \tau_\omega/\tau_U$, which should, therefore, satisfy

$$Ro_l = \frac{U}{\omega D} \gg 1.$$

The inertial scaling for flow velocity in rotating convection and numerical dynamos (Aubert *et al.* 2001; Christensen & Aubert 2006) invokes an equilibrium between the curled inertia $\nabla \times ((\mathbf{u} \cdot \nabla)\mathbf{u})$ and curled Coriolis force $\nabla \times (2\Omega \mathbf{e}_z \times \mathbf{u})$. If we assume a columnar flow and denote as δ a typical length scale for the vortices, this writes:

$$\frac{U^2}{\delta^2} \approx \frac{\Omega U}{D}$$

and, since $\omega = U/\delta$,

$$\frac{\omega}{\Omega} = \frac{\delta}{D}.$$

The Rossby number Ro_l, therefore, relates to the classical Rossby number $Ro = U/\Omega D$ through $Ro_l = Ro D/\delta$. This definition is similar to that of the local Rossby number introduced by Christensen & Aubert (2006), which was shown to be the main parameter controlling the occurrence of reversals in numerical dynamo models. It appears, therefore, plausible that the timescale competition between magnetic upwellings and magnetic vortices plays a key role in triggering polarity reversals in numerical dynamos.

We have shown that DMFI can accurately illustrate well-known macroscopic dynamo mechanisms. Furthermore, it facilitates the investigation of more complex spatio-temporal phenomena, such as

the development of magnetic upwellings, and aids interpretation of the evolution of the geomagnetic field at the CMB. Through the release of a software package publicly available upon request to the authors, we hope to make it a standard tool for future dynamo studies.

ACKNOWLEDGMENTS

REFERENCES

Alfvén, H., 1943. On the existence of electromagnetic-hydrodynamic waves, *Ark. Mat. Astron. Fys.,* **29**(2), 1–7.

Amit, H. & Olson, P., 2006. Time average and time dependent parts of core flow, *Phys. Earth planet. Int.,* **155,** 120–139, doi:10.1016/J.pepi.2005.10.006.

Aubert, J., 2005. Steady zonal flows in spherical shell dynamos, *J. Fluid. Mech.,* **542,** 53–67.

Aubert, J., Brito, D., Nataf, H.-C., Cardin, P. & Masson, J.P., 2001. A systematic experimental study of spherical shell convection in water and liquid gallium, *Phys. Earth planet. Int.,* **128,** 51–74.

Aubert, J., Amit, H. & Hulot, G., 2007. Detecting thermal boundary control in surface flows from numerical dynamos, *Phys. Earth planet. Int.,* **160,** 143–156.

Aurnou, J., Andreadis, S., Zhu, L. & Olson, P., 2003. Experiments on convection in Earth's core tangent cylinder, *Earth planet. Sci. Lett.,* **212,** 119–134.

Bloxham, J., 1986. The expulsion of magnetic flux from the Earth's core, *Geophys. J. R. astr. Soc.,* **87**(2), 669–678.

Braginsky, S.I. & Roberts, P.H., 1995. Equations governing convection in Earths core and the geodynamo, *Geophys. Astrophys. Fluid Dyn.,* **79**(1–4), 1–97.

Christensen, U. & Aubert, J., 2006. Scaling properties of convection-driven dynamos in rotating spherical shells and application to planetary magnetic fields, *Geophys. J. Int.,* **117,** 97–114.

Christensen, U. & Tilgner, A., 2004. Power requirement of the geodynamo from ohmic losses in numerical and laboratory dynamos, *Nature,* **429,** 169–171, doi:10.1038/nature02508.

Christensen, U.R. *et al.*, 2001. A numerical dynamo benchmark, *Phys. Earth planet. Int.,* **128,** 25–34.

Fearn, D.R., Roberts, P.H. & Soward, A.M., 1988. Convection, stability and the dynamo, in *Energy, Stability and Convection,* pp. 60–324, eds Galdi, G. & Staughan, B., Longman Scientific and Technical, Harlow.

Finlay, C.C., 2005. Hydromagnetic waves in Earth's core and their influence on geomagnetic secular variation, *PhD thesis*, School of Earth and Environment, University of Leeds.

Galloway, D.J. & Weiss, N.O., 1981. Convection and magnetic-fields in stars, *Astrophys. J.,* **243**(3), 945–953.

Hulot, G., Eymin, C., Langlais, B., Mandea, M. & Olsen, N., 2002. Small-scale structure of the geodynamo inferred from Oersted and Magsat satellite data, *Nature,* **416,** 620–623.

Ishihara, N. & Kida, S., 2002. Dynamo mechanism in a rotating spherical shell: competition between magnetic field and convection vortices, *J. Fluid. Mech.,* **465,** 1–32.

Jackson, A., 2003. Intense equatorial flux spots on the surface of the earth's core, *Nature,* **424**(6950), 760–763.

Jackson, A., Jonkers, A.R.T. & Walkers, M.R., 2000. Four centuries of geomagnetic secular variation from historical records, *Phil. Trans. Roy. Soc. A,* **358,** 957–990.

Kageyama, A. & Sato, T., 1997. Velocity and magnetic field structures in a magnetohydrodynamic dynamo, *Phys. Plasmas,* **4,** 1569–1575.

Kutzner, C. & Christensen, U., 2002. From stable dipolar to reversing numerical dynamos, *Phys. Earth planet. Int.,* **131,** 29–45.

Olson, P. & Amit, H., 2006. Changes in Earth's dipole, *Naturwiss.,* **93**(11), 519–542.

Olson, P. & Aurnou, J., 1999. A polar vortex in the Earth's core, *Nature,* **402,** 170–173.

Olson, P. & Christensen, U.R., 2006. Dipole moment scaling for convection-driven planetary dynamos, *Earth planet. Sci. Lett.,* **250**(3–4), 561–571.

Olson, P., Christensen, U. & Glatzmaier, G.A., 1999. Numerical modelling of the geodynamo: mechanisms of field generation and equilibration, *J. geophys. Res.,* **104**(B5), 10 383–10 404.

Roberts, P.H. & Glatzmaier, G.A., 2000. A test of the frozen-flux approximation using a new geodynamo model, *Phil. Trans. R. Soc. Lond. A,* **358**(1768), 1109–1121.

Roberts, P.H. & Scott, S., 1965. On the analysis of the secular variation. i. A hydromagnetic constraint: theory., *J. Geomag. Geoelectr.,* **17,** 137–151.

Sakuraba, A. & Kono, M., 1999. Effect of the inner core on the numerical solution of the magnetohydrodynamic dynamo, *Phys. Earth planet. Int.,* **111**(1–2), 105–121.

Sarson, G.R. & Jones, C.A., 1999. A convection driven geodynamo reversal model, *Phys. Earth planet. Int.,* **111**(1–2), 3–20.

Sreenivasan, B. & Jones, C.A., 2005. Structure and dynamics of the polar vortex in the earth's core, *Geophys. Res. Lett.,* **32**(20), L20301.

Sreenivasan, B. & Jones, C.A., 2006. Azimuthal winds, convection and dynamo action in the polar regions of planetary cores, *Geophys. Astrophys. Fluid Dyn.,* **100**(4-5), 319–339.

Valet, J.P. & Meynadier, L., 1993. Geomagnetic field intensity and reversals during the past four million years., *Nature,* **336,** 234–238.

Weiss, N.O., 1966. The expulsion of magnetic flux by eddies, *Proc. R. Soc. Lond. A.,* **293**(1434), 310–328.

Wicht, J., 2002. Inner-core conductivity in numerical dynamo simulations, *Phys. Earth planet. Int.,* **132,** 281–302.

Wicht, J., 2005. Palaeomagnetic interpretation of dynamo simulations, *Geophys. J. Int.,* **162,** 371–380.

Wicht, J. & Olson, P., 2004. A detailed study of the polarity reversal mechanism in a numerical dynamo model, *Geophys. Geochem. Geosystems.,* **5**(3).